

Three-dimensional Magnetic Reconnection Triggering an X-class Confined Flare in Active Region 12192

Ting Li^{1,2}, Yijun Hou^{1,2}, Shuhong Yang^{1,2} & Jun Zhang^{1,2}

ABSTRACT

We present an extensive analysis of the X2.0-class confined flare on 2014 October 27 in the great active region AR 12192, observed by the *Interface Region Imaging Spectrograph* and the *Solar Dynamics Observatory*. The slipping motion of the substructures within the negative-polarity flare ribbon (R1) and continual reconnection-induced flows during the confined flare are first presented. The substructures within ribbon R1 were observed to slip in opposite directions at apparent speeds of 10-70 km s⁻¹. The slipping motion exhibited the quasi-periodic pattern with a period of 80-110 s, which can be observed since the flare start and throughout the impulsive phase of the flare. Simultaneously quasi-periodic flows moved along a reverse-S shaped filament, with an average period of about 90 s. The period of reconnection-induced flows is similar to that of the slippage of ribbon substructures, implying the occurrence of quasi-periodic slipping magnetic reconnection. The spectral observations showed that the Si IV line was blueshifted by 50-240 km s⁻¹ at the location of the flows. During the process of the flare, the filament did not show the rise phase and was not associated with any failed eruption. The flare mainly consisted of two sets of magnetic systems, with both of their east ends anchoring in ribbon R1. We suggest that the slipping magnetic reconnection between two magnetic systems triggers the confined flare.

Subject headings: magnetic reconnection—Sun: activity—Sun: flares—Sun: magnetic fields

1. Introduction

Solar flares are explosive manifestations of magnetic energy in the solar corona (Forbes et al. 2006). The eruptive flares are associated with coronal mass ejections (CMEs) that

¹CAS Key Laboratory of Solar Activity, National Astronomical Observatories, Chinese Academy of Sciences, Beijing 100101, China; liting@nao.cas.cn

²School of Astronomy and Space Science, University of Chinese Academy of Sciences, Beijing 100049, China

constitute major drivers for space weather (Svestka & Cliver 1992). The confined flares are not accompanied by CMEs, however, they are important to reveal the physical nature of solar flares and the relationship between flares and CMEs.

Many previous studies have attempted to explain why a flare develops into a confined event (Gorbachev & Somov 1989; Schmieder et al. 1997; Nindos & Andrews 2004; Yang et al. 2014; Dalmasse et al. 2015; Jing et al. 2015; Liu et al. 2014). Among the reported confined flares, one category is related to loop-loop interactions, which will not lead to CMEs due to the absence of a filament or flux rope as the seed of a CME (Green et al. 2002; Sui et al. 2006; Ning et al. 2018). This kind of confined flares often shows brightenings in compact loop system, and has short time scales (e.g., on the order of a few minutes) and small size scales (Pallavicini et al. 1977). The other category of confined flares is attributed to high strength and low decay index of the background magnetic field that prevent magnetic energy release (Fan & Gibson 2007; Cheng et al. 2011; Zuccarello et al. 2017), and either the filament fails to erupt (Ji et al. 2003; Guo et al. 2012; Kushwaha et al. 2015) or the filament successfully erupts and no material is ejected into the interplanetary space (Yang & Zhang 2018; Li et al. 2018). Török & Kliem (2005) simulated a confined eruption driven by the kink instability of a coronal magnetic flux rope, and suggested that the gradual decrease of the overlying field with height was a main cause of confined flares. Wang & Zhang (2007) statistically investigated the X-class flares occurring during 1996–2004 and found that the confined flares (about 10%) occurred closer to the magnetic center, which implied that a stronger overlying constraining field may determine whether a flare is confined.

Magnetic reconnection is believed to be the fundamental process that converts the stored magnetic energy into kinetic energy of accelerated particles and plasma and thermal energy during a flare (Priest & Forbes 2002). In the classical 2D picture, magnetic reconnection can occur at null points, where the magnetic field vanishes (Lau & Finn 1990; Wang 1997). In 3D, the quasi-separatrix layers (QSLs; Démoulin et al. 1996), i.e., thin layers characterized by very strong magnetic connectivity gradients, are also preferred sites for current accumulation and energy dissipation (Mandrini et al. 1997; Pontin et al. 2016). In the 3D reconnecting mode, magnetic field lines “slip” or “flip” inside the plasma due to the continuous exchange of magnetic connectivity, and thus the magnetic reconnection occurring in the QSLs is referred as slipping magnetic reconnection if the speed of slipping motion is sub-Alfvénic (Priest & Démoulin 1995; Aulanier et al. 2006). The footprints of the QSLs have been shown to coincide with the observed flare ribbons (Démoulin et al. 1997; Dalmasse et al. 2015; Savcheva et al. 2015). The motions of ultraviolet (UV) brightening along the ribbons are considered as important signatures of slipping magnetic reconnection along the QSLs (Aulanier et al. 2006; Janvier et al. 2013). In recent years, several studies have found the evidence of slipping magnetic reconnection during eruptive flares (Dudík et al. 2014, 2016;

Li & Zhang 2014, 2015; Zheng et al. 2016; Jing et al. 2017). Li et al. (2015) showed the quasi-periodic slipping motion of bright kernels within flare ribbons, suggestive of the occurrence of quasi-periodic slipping magnetic reconnection during an eruptive flare. Dudík et al. (2016) presented that the flare loops slipped in opposite directions along flare ribbons, consistent with the prediction of the standard solar flare model in 3D (Aulanier et al. 2012; Janvier et al. 2014).

Until now, the detailed signatures of slipping magnetic reconnections have been presented only in eruptive flares. How about the confined flares? Can the slipping magnetic reconnection trigger the confined flares? Why does the flare develop into a confined event? In this paper, based on the observations from the *Interface Region Imaging Spectrograph* (*IRIS*; De Pontieu et al. 2014) and the *Solar Dynamics Observatory* (*SDO*; Pesnell et al. 2012), we investigate in detail the features of the 3D reconnection process during a confined X2.0 flare on 2014 October 27 in the great solar active region (AR) 12192. Especially, the slipping motion of the substructures within a flare ribbon and continual reconnection-induced flows during the confined flare are first presented.

NOAA AR 12192 was the biggest sunspot region in solar cycle 24, and it produced 6 X-class flares, 22 M-class flares, and 53 C-class flares during its disk passage. Interestingly, all the X-class flares in the AR are confined flares and not associated with any CMEs. Previous studies showed that AR 12192 exhibited weaker non-potentiality and stronger confinement from the overlying magnetic field, which determine the poor CME productivity of the AR (Sun et al. 2015; Chen et al. 2015; Liu et al. 2016; Sarkar & Srivastava 2018). However, Zhang et al. (2017) suggested that the complexity of the involved magnetic field structures may be responsible for the confined nature. The strongest X3.1-class flare on 2014 October 24 has been extensively studied by using nonlinear force-free field (NLFFF) extrapolations and numerical simulations. Inoue et al. (2016) and Jiang et al. (2016) suggested that the AR was composed of multiple weak-twisted flux tubes and the tether-cutting reconnection between these sheared arcades triggered the X3.1-class flare. Prasad et al. (2018) attributed the flare onset to the null-point reconnections in a fan-spine topology, and they found no flux rope was involved in the flare. Contrarily, a magnetic flux rope was present in the numerical simulation of Amari et al. (2018), who suggested that a strong magnetic cage of overlying field could explain the confined nature.

The structure of the paper is as follows. In Section 2, we describe the *IRIS* and *SDO* observations and the methods of data analysis. Section 3 presents the dynamic evolution of flare loops and ribbons, and the flows along a non-eruptive filament. Finally, in Section 4, we discuss and summarize our work.

2. Observations and Data Analysis

In this study, we focus on the last X-class flare in AR 12192 occurring near the west limb (S18°, W57°) on 2014 October 27. The event has been analyzed by Polito et al. (2016), who investigated the dynamics of the chromospheric plasma at the flare kernels. The soft X-ray light curve from the Geostationary Operational Environment Satellite (GOES) 1–8 Å channel shows that the X2.0-class flare started at 14:12 UT, peaked at 14:47 UT and ended at 15:09 UT. The *IRIS* performed an eight-step coarse raster observation from 14:04 UT to 17:44 UT, with the step of 2'', giving a total field of view (FOV) of 14'' × 119'' for the spectra. The step cadence of the spectral observation was ~3.2 s and each raster lasted for about 26 s. The *IRIS* slit jaw images (SJIs) were taken at a cadence of 13 s in the wavelengths 1330 Å (at steps 0, 4), 2796 Å (at steps 1, 5) and 2832 Å (at steps 3, 7). The spatial pixel size of the images is ~0''.332. We mainly use the 1330 Å SJIs to investigate the detailed evolution of flare ribbons. The 1330 Å filter records emission mainly from the UV continuum and two C II lines, which are formed in the lower transition region (TR) with a temperature of about 25000 K (Tian et al. 2014). The spectral observations of Si IV 1402.77 Å window are mainly analyzed in our study. The Si IV 1402.77 Å profile samples gas at ~80000 K equilibrium temperatures in the middle TR (Peter et al. 2014). We apply the single-Gaussian fit to obtain the Doppler shift and the line width (1/e width). The non-thermal width is also calibrated by assuming the thermal broadening of 6.88 km s⁻¹ (T_e=80000 K of Si IV line) and the instrumental broadening of 4.1 km s⁻¹ (De Pontieu et al. 2014).

We also use the E(UV) images from the Atmospheric Imaging Assembly (AIA; Lemen et al. 2012) and line-of-sight (LOS) magnetograms from the Helioseismic and Magnetic Imager (HMI; Scherrer et al. 2012) on board the *SDO*. The AIA instrument observes the Sun in 10 UV/EUV filters with the cadences of 24/12 s and the pixel size of 0''.6. We focus on several different filters including 1600, 304, 171 and 131 Å to fully understand the dynamic evolution of the flare and a non-eruptive filament during the flare. The HMI LOS magnetograms are used to reveal the magnetic structures where flare ribbons are located. We co-align the AIA images and *IRIS* 1330 Å SJIs by identifying the characteristic features.

3. Results

3.1. Overview of the Event

As shown from the high-temperature 131 Å observations (about 11 MK; O’Dwyer et al. 2010), the flare loops displayed a clear “X shape” in the initial stage of the flare (Figures 1(a) and (b); also see the animation of Figure 1). Two curved flare ribbons R1 and R2 were

formed as seen in 1600 Å images (Figure 1(d)). The east footpoints of the X-shaped flare loops were located at ribbon R1 and their west footpoints anchored in ribbon R2. Then the east footpoints of the “X-shaped” structure S1 elongated northward and meanwhile another large-scale structure S2 appeared, connecting ribbon R1 and a new ribbon R3 (Figures 1(b) and (e)). Afterwards, the east footpoints (R1) of the structure S2 slipped towards the south while the west footpoints (R3) slipped in the opposite direction (red arrows in Figure 1(c)). The comparison of 1600 Å images with HMI LOS magnetograms showed that ribbon R1 was located at the negative-polarity sunspot, ribbon R2 at the leading positive-polarity fields of the AR, and ribbon R3 anchoring at the peripheral positive-polarity fields (Figure 1(f)).

3.2. Dynamics of Flare Loops and Flare Ribbons

The 171 Å and 304 Å observations showed that a “reverse S-shaped” filament existed between the two flare ribbons R1 and R2 (Figures 2(a)-(b); also see the animation of Figure 2), with a length of about 70 Mm. The initial brightenings at the east part of the filament appeared from about 8 min after the flare onset (14:20 UT; see Figure 2(c)), indicating that the reconnection during the flare resulted in the brightenings and activation of the filament. Then the entire filament was brightened and seemed to undergo a tiny torsional deformation (Figure 2(d)). Continual mass flows were observed from the middle part of the filament to the east end (Figure 2(d)), implying the occurrence of magnetic reconnection between the filament and the nearby magnetic structures. The filament showed no evident rise during the whole event and still existed at the end of the flare.

The detailed evolution of flare ribbons can be obtained from the *IRIS* 1330 Å observations. The ribbon R1 showed an elongation motion towards the north almost from the flare start (red arrows in Figures 2(e)-(g)). Meanwhile, the bright substructures within ribbon R1 exhibited a slipping motion in the opposite direction (brown circles and arrows in Figures 2(f)-(g)). Associated with the elongation of the negative-polarity ribbon R1, the positive-polarity ribbon R2 also showed an elongation motion towards the south (blue arrows in Figures 2(e)-(g)). Simultaneously, the separation between ribbons R1 and R2 increased as they moved away from the polarity inversion line. As ribbon R1 reached the eastern footpoints of the filament, the filament material was illuminated in the 1330 Å image (Figure 2(g)) and continual reconnection-induced flows were detected along the non-eruptive filament (Figure 2(h)). The high-temperature flare loops connecting the two ribbons R1 and R2 were traced out in the 131 Å images (Figures 2(i)-(k)). Two flare loops L1 and L2 comprised the “X shape” in the initial stage (Figure 2(i)), with their east end at ribbon R1 and west end at ribbon R2. Associated with the elongation motions of ribbons R1 and R2 in

opposite directions, more flare loops (L3 and L4 in Figures 2(j)-(k)) were traced out in the 131 Å observations. These flare loops at different times (Figure 2(k)) delineated a “bi-fan” surface (Li & Zhang 2014), implying the complicated magnetic structure involved in the flare (Polito et al. 2016). The comparison of the 1330 Å and 131 Å images shows that the 1330 Å substructures within the evolving ribbon are nearly cospatial with the footpoints of the 131 Å loops. The relationship between the flare kernels observed in 1600 Å or 1700 Å and the high-temperature flare loops has already been reported in Dudík et al. (2014, 2016). The emission intensity of the flare loops was enhanced significantly as the flare developed, and the reconnection-induced flows seemed to originate from the highly sheared location (Figure 2(l)).

The 1330 Å observations showed that the east ribbon R1 was composed of numerous dot-like substructures, which slipped in opposite directions towards both ends of the ribbon (Figure 3 and the associated animation). We followed the trails of 5 different substructures within ribbon R1 and displayed them in Figure 3. Almost from the flare start, bright dot “1” showed the apparent slipping motion towards the straight part (SP in panel (g)) of the ribbon, with a displacement of about 12 Mm in 3 min and an average speed of 70 km s^{-1} (panels (a)-(c)). However, bright dots “2” and “3” slipped towards the hook of the ribbon at a slower speed of about 20 km s^{-1} (panels (d)-(f)). Similarly, bright dots “4” and “5” moved in opposite directions (panels (g)-(i)), and the bi-directional slippage can be observed until the flare peak time (panel (i)).

In order to analyze the slipping motions of the substructures, we obtain the stack plot (Figure 4(a)) along slice “A–B” in 1330 Å images (red curve in Figure 3(g)). As seen from the stack plot, multiple bright stripes were detected, with each stripe representing the apparent slipping motion of one single substructure. The speed of the slipping motion was about $20\text{-}30 \text{ km s}^{-1}$ in the first stage before 14:35 UT. Then the substructures within ribbon R1 were illuminated again, implying the occurrence of two-step energy release in the event. In the second stage after 14:35 UT, the majority of the substructures exhibited the slipping motion from “B” to “A” and a small fraction was seen to slip in the opposite direction, with apparent speeds of $10\text{-}40 \text{ km s}^{-1}$. Along two horizontal slices (“H1” and “H2” in Figure 4(a)), we also obtain the intensity-time profiles (black and red curves in Figure 4(b)) at two certain locations. The two profiles both showed the quasi-periodic pattern, indicating that at the same location the substructure intermittently appeared and passed by. The average period of the slipping motion was about 110 s in the first stage and 80 s in the second episode. The slipping motion lasted about 30 min and was observed throughout the impulsive phase of the flare (Figure 4(b)). The spatial size of the substructures was estimated as about 500 km (Figures 4(c)-(d)), comparable to the resolution limit of the *IRIS* instrument of about 480 km. The substructures observed in 1330 Å are larger than the fine structures within $\text{H}\alpha$

flare ribbons in another event (~ 100 km in Sharykin & Kosovichev 2014). The difference is probably caused by the low spatial resolution of the *IRIS* observations compared to the high-resolution $H\alpha$ images.

3.3. Reconnection-induced Flows Along the Non-eruptive Filament

About 8 min after the flare onset ($\sim 14:20$ UT), the reverse-S shaped filament was activated and continual mass flows appeared from its middle part to the east end. Along the main axis of the filament, we obtained two stack plots (Figures 5(c)-(d)) respectively along slice “C-D” in 1330 Å images (red curve in Figure 5(a)) and slice “E-F” in 304 Å images (blue curve in Figure 5(b)). As seen from the 1330 Å stack plot (Figure 5(c)), the mass flows started at about 14:20 UT and continued in the gradual phase of the flare. The duration of mass flows was more than 40 min and the projected velocity in the plane of the sky was 50-75 km s⁻¹. The flows were generated intermittently and showed a quasi-periodic pattern with an average period of about 90 s (brown curve in Figure 5(c)). In addition, at about 14:25 UT, a secondary flare ribbon SR (Polito et al. 2016) appeared between ribbons R1 and R2 and elongated towards ribbon R2 at a speed of 90 km s⁻¹ (Figures 5(a)-(c)). From the 304 Å stack plot (Figure 5(d)), the long-duration flows can also be clearly displayed, which moved at a speed of 60-110 km s⁻¹.

The *IRIS* spectral observations of Si IV 1402.77 Å line cover the east part of the filament and the reconnection-induced flows. The locations of Slit 0, Slit 4 and Slit 7 are focused on (Figures 6(a) and (d)) and their spectral images of the Si IV 1402.77 Å line at two different times are displayed in Figures 6(b1)-(b3) and (e1)-(e3). The Si IV line exhibited evident blueshifts at the locations of the flows along the three slits. At 14:28:57 UT, the spectral tilt was clearly visible at the location of Slit 0 (Figure 6(b1)), suggestive of the spinning motion along the magnetic structure of the filament (Curdt et al. 2012; Li et al. 2014). The 1330 Å SJIs show that the top edge of the intersection area between the slit locations and the filament seems to be along the same fine structure of the filament (FS in Figures 6(a) and (d)). Three different locations “A”, “B” and “C” along FS are selected, and their spectral profiles and corresponding single-Gaussian fits are shown in Figures 6(c) and (f). For the location “A”, the calculated blueshift reached about 121 km s⁻¹ and the non-thermal width was 61 km s⁻¹ at 14:28:57 UT (Figure 6(c)). For the locations closer to the reconnection region (“B” and “C”), the blueshifts decreased and the non-thermal widths remained the same. The blueshift at location “B” decreased to 82 km s⁻¹ and location “C” at the west had a blueshift of only 64 km s⁻¹. At 14:38:17 UT, the blueshift at location “A” increased to 143 km s⁻¹ with a large non-thermal width of about 150 km s⁻¹ (Figure 6(f)). Similarly, the

Doppler shifts at the locations near the reconnection site are smaller than those locations far away. The difference of Doppler shifts along the same fine structure probably implies the helical magnetic field of the filament.

In order to analyze the temporal evolution of Doppler shifts and non-thermal widths at the reconnection-induced flows, we fit the Si IV 1402.77 Å profiles and obtained the stack plots of peak intensity, Doppler shift and non-thermal width along Slit 0 and Slit 4 (Figure 7). Ribbon R2 showed an evident separation motion with a speed of about 18 km s^{-1} , however, ribbon R1 located in the sunspot did not show significant displacement perpendicular to the ribbon (Figures 7(a) and (d)). The Si IV emission exhibited obvious redshifts of 20-90 km s^{-1} at ribbon R2 (Figures 7(b) and (e)), suggestive of the chromospheric condensation during the process of explosive chromospheric evaporation (Fisher et al. 1985; Zhang et al. 2016; Li et al. 2017). At ribbon R1, the Si IV line was blueshifted by about 10-20 km s^{-1} , probably due to the combination effect of the chromospheric condensation and the reconnection-induced flows at the footpoints of the filament. About 8 min after the flare onset, the Doppler blueshifts and broadening at the location of flows appeared, with the blueshift of 50-240 km s^{-1} (Figures 7(b) and (e)) and the non-thermal width reaching about 60-120 km s^{-1} (Figures 7(c) and (f)). The blueshift lasted for more than 40 min and can be observed throughout the impulsive and gradual phases of the flare.

4. Summary and Discussion

We have presented an extensive analysis of an X2.0-class confined flare in AR 12192 on 2014 October 27. The flare mainly consisted of two sets of magnetic systems, with their east ends anchoring in the same negative-polarity ribbon (R1) above a sunspot umbra. The west ends of the two magnetic systems were respectively located in other two positive-polarity ribbons (R2 and R3). Using the *IRIS* high-resolution observations, we report the apparent slipping motion of ribbon substructures along ribbon R1 in the TR. The majority of the substructures exhibited the slipping motion towards the hook of ribbon R1 away from the inversion line and a small fraction was seen to slip in the opposite direction towards the straight part of R1, with apparent speeds of 10-70 km s^{-1} . At the same location, the substructures intermittently appeared with a period of 80-110 s, indicating the quasi-periodic pattern of the slippage. The slipping motion can be observed since the flare start and throughout the impulsive phase of the flare. A reverse-S shaped filament connecting ribbons R1 and R2 was activated when the slippage along ribbon R1 reached the end of the filament. Simultaneously continual reconnection-induced flows moved along the filament from its middle part to the east end, with a speed of 50-110 km s^{-1} in the plane of the

sky. The flows were generated quasi-periodically with an average period of about 90 s. The period of the flows is similar to that of the slipping motion of ribbon substructures, implying the occurrence of quasi-periodic slipping magnetic reconnection. The spectral observations showed that at the reconnection-induced flows the Si IV line was blueshifted by 50-240 km s⁻¹ and broadened with the non-thermal width reaching about 60-120 km s⁻¹. The Doppler blueshifts lasted for about 40 min and can be observed until the gradual phase of the flare. During the process of the flare, the filament did not show evident rise phase and did not erupt at all.

During this flare, the magnetic field line linkage has two basic sets of magnetic connectivities (S1 and S2), with their east ends both anchoring in negative-polarity ribbon R1 and their respective west ends in two positive-polarity ribbons R2 and R3. The bi-directional slipping motion of ribbon R1 and the simultaneous elongations of ribbons R2 and R3 imply the existence of a QSL surface between the two magnetic systems (S1 and S2). We suggest that the magnetic reconnection occurs along the QSL and causes the continuous exchange of connectivities of two magnetic systems S1 and S2, which results in apparent slippage of the entire reconnecting field lines. The QSL reconnection also generates the observed flows along the non-eruptive filament. According to the connectivity of the filament, we suggest that the filament belongs to system S1. When the slippage of R1 reached the eastern end of the filament, the slipping reconnection between field lines of the filament and system S2 occurred along the QSL and caused the quasi-periodic flows along the filament. A relevant simulation study was carried out by Aulanier et al. (2005), who performed the MHD simulations of the development of electric currents in bipolar configurations. In that study, two sets of magnetic connectivities appeared in the bipolar potential configurations and slipping magnetic reconnection occurred along the QSL between the two systems (see their Figure 3), similar to the magnetic topology in our observations.

The bi-directional slippage of the substructures within the same flare ribbon in the TR is first reported in this study. We suggest that the slipping substructures in two directions respectively correspond to the footpoints of two magnetic systems. The continuous slipping magnetic reconnection between the two magnetic systems results in the exchange of their connectivities and the slippage of reconnecting field lines in opposite directions. Using the *SDO/AIA* observations, Dudík et al. (2016) reported the apparent slipping motions of flare loops in opposite directions during an eruptive flare. They interpreted the slippage towards the ribbon hook corresponding to the field lines of the erupting flux rope and the slippage in the opposite direction corresponding to the flare loops, fulfilling the prediction of the standard solar flare model in 3D. Different from their observations, there is no erupting flux rope involved in the analyzed confined flare and our observations can not be explained by the 3D standard flare model. Similar to the behavior of ribbons substructures in the TR,

the chromospheric knots within a ribbon-like structure have also been observed to move in two directions towards both ends of the ribbon (Sobotka et al. 2016). These observations imply that the energy release by slipping magnetic reconnection can affect both the TR and the chromosphere.

The quasi-periodic property of slipping kernels within flare ribbons has been revealed during an eruptive flare by Li & Zhang (2015), and was further verified by Brosius & Daw (2015) and Brannon et al. (2015). All these observations about the sawtooth oscillation of ribbon substructures are for eruptive flares, and the reported period range is between 90 s and 300 s. In our observations, the small-scale substructures (~ 500 km) within flare ribbons also exhibit the quasi-periodic slipping motion in the confined flare, and the oscillation period of 80-110 s is similar to that during eruptive flares. Recently, Parker & Longcope (2017) proposed a model of the tearing mode instability and reproduced the observational signatures of the sawtooth oscillation. They suggested that a tearing mode with asymmetric shear flow occurring at a current sheet produced fluid motions similar to the observations. Another explanation about the sawtooth oscillation of ribbon substructures is related to the modulation of MHD waves (McLaughlin et al. 2009; Nakariakov & Melnikov 2009). The MHD waves during the flare may affect the reconnection site and cause the oscillatory magnetic reconnection.

The simultaneous imaging and spectroscopic observations of the reconnection-induced flows in the confined flare are presented in this work. The flows moved along the QSLs at a speed of 50-240 km s⁻¹ in the impulsive and gradual phases of the flare. Here, the flows should not be confused with the downflows along post-flare loops due to the material cooling after magnetic reconnections (Schmieder et al. 1996; Song et al. 2016). The appearance of reconnection-induced flows in confined flares differ from that in eruptive flares. In eruptive flares, bi-directional outflows are usually in forms of plasmoid ejections and contracting cusp-shaped loops at speeds of about 100-300 km s⁻¹ (Savage & McKenzie 2011; Liu et al. 2013), comparable to the Doppler shifts of reconnection-induced flows in our event. Moreover, the filament involved in the flare seemed to take part in the QSL reconnection, however, was still present after the flare. It did not show the rise phase and was not associated with any failed eruption. The appearance of the filament and the reconnection-induced flows could not be explained by the classical picture of confined flares, either due to a failed filament eruption (Ji et al. 2003; Kushwaha et al. 2015) or the loop-loop interaction (Green et al. 2002; Ning et al. 2018). Thus the physical factors determining the likelihood of ejective/confined eruptions need to be revisited. We suggest that the QSL reconnection in complex magnetic configuration caused no significant topological change, and thus the stability of the filament was not destroyed and the flare eventually developed into a confined event.

We thank Miho Janvier for useful discussions. *SDO* is a mission of NASA’s Living With a Star Program. *IRIS* is a NASA small explorer mission developed and operated by LMSAL with mission operations executed at NASA’s Ames Research center and major contributions to downlink communications funded by the Norwegian Space Center (NSC, Norway) through an ESA PRODEX contract. This work is supported by the National Natural Science Foundations of China (11773039, 11533008, 11790304, 11673035, 11673034 and 11790300), Key Programs of the Chinese Academy of Sciences (QYZDJ-SSW-SLH050), and the Youth Innovation Promotion Association of CAS (2017078 and 2014043).

REFERENCES

- Amari, T., Canou, A., Aly, J.-J., Delyon, F., & Alauzet, F. 2018, *Nature*, 554, 211
- Aulanier, G., Janvier, M., & Schmieder, B. 2012, *A&A*, 543, A110
- Aulanier, G., Pariat, E., & Démoulin, P. 2005, *A&A*, 444, 961
- Aulanier, G., Pariat, E., Démoulin, P., & DeVore, C. R. 2006, *Sol. Phys.*, 238, 347
- Brannon, S. R., Longcope, D. W., & Qiu, J. 2015, *ApJ*, 810, 4
- Brosius, J. W., & Daw, A. N. 2015, *ApJ*, 810, 45
- Chen, H., Zhang, J., Ma, S., et al. 2015, *ApJ*, 808, L24
- Cheng, X., Zhang, J., Ding, M. D., Guo, Y., & Su, J. T. 2011, *ApJ*, 732, 87
- Curdt, W., Tian, H., & Kamio, S. 2012, *Sol. Phys.*, 280, 417
- Dalmasse, K., Chandra, R., Schmieder, B., & Aulanier, G. 2015, *A&A*, 574, A37
- Démoulin, P., Bagala, L. G., Mandrini, C. H., Henoux, J. C., & Rovira, M. G. 1997, *A&A*, 325, 305
- Démoulin, P., Priest, E. R., & Lonie, D. P. 1996, *J. Geophys. Res.*, 101, 7631
- De Pontieu, B., Title, A. M., Lemen, J. R., et al. 2014, *Sol. Phys.*, 289, 2733
- Dudík, J., Janvier, M., Aulanier, G., et al. 2014, *ApJ*, 784, 144
- Dudík, J., Polito, V., Janvier, M., et al. 2016, *ApJ*, 823, 41
- Fan, Y., & Gibson, S. E. 2007, *ApJ*, 668, 1232

- Fisher, G. H., Canfield, R. C., & McClymont, A. N. 1985, *ApJ*, 289, 414
- Forbes, T. G., Linker, J. A., Chen, J., et al. 2006, *Space Sci. Rev.*, 123, 251
- Gorbachev, V. S., & Somov, B. V. 1989, *Soviet Ast.*, 33, 57
- Green, L. M., Matthews, S. A., van Driel-Gesztelyi, L., Harra, L. K., & Culhane, J. L. 2002, *Sol. Phys.*, 205, 325
- Guo, Y., Ding, M. D., Schmieder, B., Démoulin, P., & Li, H. 2012, *ApJ*, 746, 17
- Inoue, S., Hayashi, K., & Kusano, K. 2016, *ApJ*, 818, 168
- Janvier, M., Aulanier, G., Bommier, V., et al. 2014, *ApJ*, 788, 60
- Janvier, M., Aulanier, G., Pariat, E., & Démoulin, P. 2013, *A&A*, 555, A77
- Ji, H., Wang, H., Schmahl, E. J., Moon, Y.-J., & Jiang, Y. 2003, *ApJ*, 595, L135
- Jiang, C., Wu, S. T., Yurchyshyn, V., et al. 2016, *ApJ*, 828, 62
- Jing, J., Liu, R., Cheung, M. C. M., et al. 2017, *ApJ*, 842, L18
- Jing, J., Xu, Y., Lee, J., et al. 2015, *Research in Astronomy and Astrophysics*, 15, 1537
- Kushwaha, U., Joshi, B., Veronig, A. M., & Moon, Y.-J. 2015, *ApJ*, 807, 101
- Lau, Y.-T., & Finn, J. M. 1990, *ApJ*, 350, 672
- Lemen, J. R., Title, A. M., Akin, D. J., et al. 2012, *Sol. Phys.*, 275, 17
- Li, D., Ning, Z. J., Huang, Y., & Zhang, Q. M. 2017, *ApJ*, 841, L9
- Li, L. P., Peter, H., Chen, F., & Zhang, J. 2014, *A&A*, 570, A93
- Li, T., Yang, S., Zhang, Q., Hou, Y., & Zhang, J. 2018, *ApJ*, 859, 122
- Li, T., & Zhang, J. 2014, *ApJ*, 791, L13
- Li, T., & Zhang, J. 2015, *ApJ*, 804, L8
- Liu, L., Wang, Y., Wang, J., et al. 2016, *ApJ*, 826, 119
- Liu, R., Titov, V. S., Gou, T., et al. 2014, *ApJ*, 790, 8
- Liu, W., Chen, Q., & Petrosian, V. 2013, *ApJ*, 767, 168

- McLaughlin, J. A., De Moortel, I., Hood, A. W., & Brady, C. S. 2009, *A&A*, 493, 227
- Mandrini, C. H., Demoulin, P., Bagala, L. G., et al. 1997, *Sol. Phys.*, 174, 229
- Nakariakov, V. M., & Melnikov, V. F. 2009, *Space Sci. Rev.*, 149, 119
- Nindos, A., & Andrews, M. D. 2004, *ApJ*, 616, L175
- Ning, H., Chen, Y., Wu, Z., et al. 2018, *ApJ*, 854, 178
- O’Dwyer, B., Del Zanna, G., Mason, H. E., Weber, M. A., & Tripathi, D. 2010, *A&A*, 521, A21
- Pallavicini, R., Serio, S., & Vaiana, G. S. 1977, *ApJ*, 216, 108
- Parker, J., & Longcope, D. 2017, *ApJ*, 847, 30
- Pesnell, W. D., Thompson, B. J., & Chamberlin, P. C. 2012, *Sol. Phys.*, 275, 3
- Peter, H., Tian, H., Curdt, W., et al. 2014, *Science*, 346, 1255726
- Polito, V., Reep, J. W., Reeves, K. K., et al. 2016, *ApJ*, 816, 89
- Pontin, D., Galsgaard, K., & Démoulin, P. 2016, *Sol. Phys.*, 291, 1739
- Prasad, A., Bhattacharyya, R., Hu, Q., Kumar, S., & Nayak, S. S. 2018, *ApJ*, 860, 96
- Priest, E. R., & Démoulin, P. 1995, *J. Geophys. Res.*, 100, 23443
- Priest, E. R., & Forbes, T. G. 2002, *A&A Rev.*, 10, 313
- Sarkar, R., & Srivastava, N. 2018, *Sol. Phys.*, 293, 16
- Savage, S. L., & McKenzie, D. E. 2011, *ApJ*, 730, 98
- Savcheva, A., Pariat, E., McKillop, S., et al. 2015, *ApJ*, 810, 96
- Scherrer, P. H., Schou, J., Bush, R. I., et al. 2012, *Sol. Phys.*, 275, 207
- Schmieder, B., Aulanier, G., Demoulin, P., et al. 1997, *A&A*, 325, 1213
- Schmieder, B., Heinzl, P., van Driel-Gesztelyi, L., & Lemen, J. R. 1996, *Sol. Phys.*, 165, 303
- Sharykin, I. N., & Kosovichev, A. G. 2014, *ApJ*, 788, L18
- Sobotka, M., Dudík, J., Denker, C., et al. 2016, *A&A*, 596, A1

- Song, Q., Wang, J.-S., Feng, X., & Zhang, X. 2016, *ApJ*, 821, 83
- Sui, L., Holman, G. D., & Dennis, B. R. 2006, *ApJ*, 646, 605
- Sun, X., Bobra, M. G., Hoeksema, J. T., et al. 2015, *ApJ*, 804, L28
- Svestka, Z., & Cliver, E. W. 1992, in *IAU Colloq. 133, Eruptive Solar Flares*, Vol. 399, ed. Z. Svestka, B. V. Jackson, & M. E. Machado (New York: Springer), 1
- Tian, H., DeLuca, E. E., Cranmer, S. R., et al. 2014, *Science*, 346, 1255711
- Török, T., & Kliem, B. 2005, *ApJ*, 630, L97
- Wang, H. 1997, *Sol. Phys.*, 174, 265
- Wang, Y., & Zhang, J. 2007, *ApJ*, 665, 1428
- Yang, S., & Zhang, J. 2018, *ApJ*, 860, L25
- Yang, S., Zhang, J., & Xiang, Y. 2014, *ApJ*, 793, L28
- Zhang, J., Li, T., & Chen, H. 2017, *ApJ*, 845, 54
- Zhang, Q. M., Li, D., Ning, Z. J., et al. 2016, *ApJ*, 827, 27
- Zheng, R., Chen, Y., & Wang, B. 2016, *ApJ*, 823, 136
- Zuccarello, F. P., Chandra, R., Schmieder, B., Aulanier, G., & Joshi, R. 2017, *A&A*, 601, A26

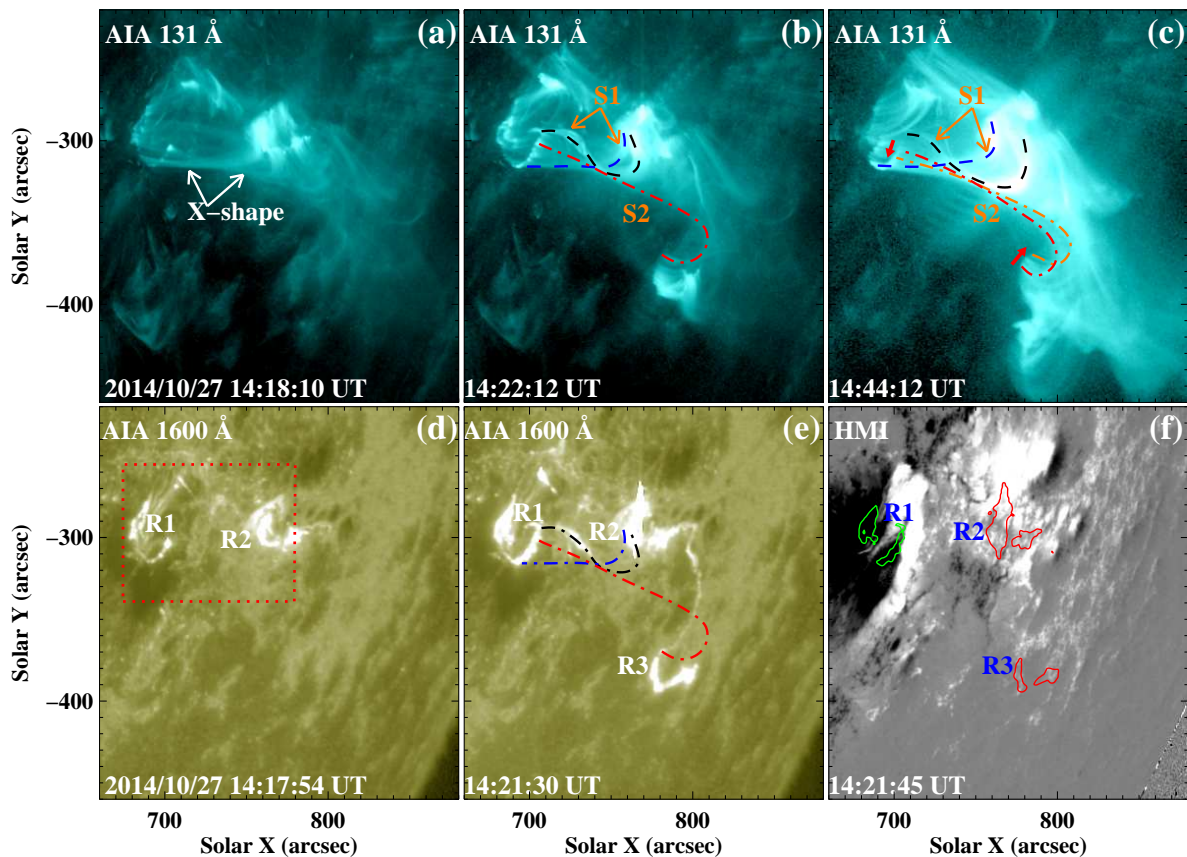


Fig. 1.— Overview of the confined X2.0 flare on 2014 October 27 in AR 12192 including the multi-wavelength images from *SDO/AIA* and *SDO/HMI* LOS magnetogram. The structure S1 denotes the “X-shaped” flare loops outlined by black and blue dashed curves. The red and brown dash-dotted curves show another set of magnetic structure S2 involved in the flare. The red arrows in panel (c) represent the two opposite slipping directions of the footpoints of structure S2. The duplications of structures S1 and S2 are also shown in panel (e). The red rectangle in panel (d) shows the FOV of the images in Figure 2. R1, R2 and R3 are three flare ribbons, and their brightness contours in AIA 1600 Å image are shown in panel (f). In the associated animation, the AIA 131 Å and AIA 1600 Å image animations start at 14:05:20 UT and 14:05:04 UT, respectively. They end at 15:29:47 UT and 15:29:28 UT. The HMI magnetograms are not included in the animation since the evolution of magnetic fields is not evident during this period.

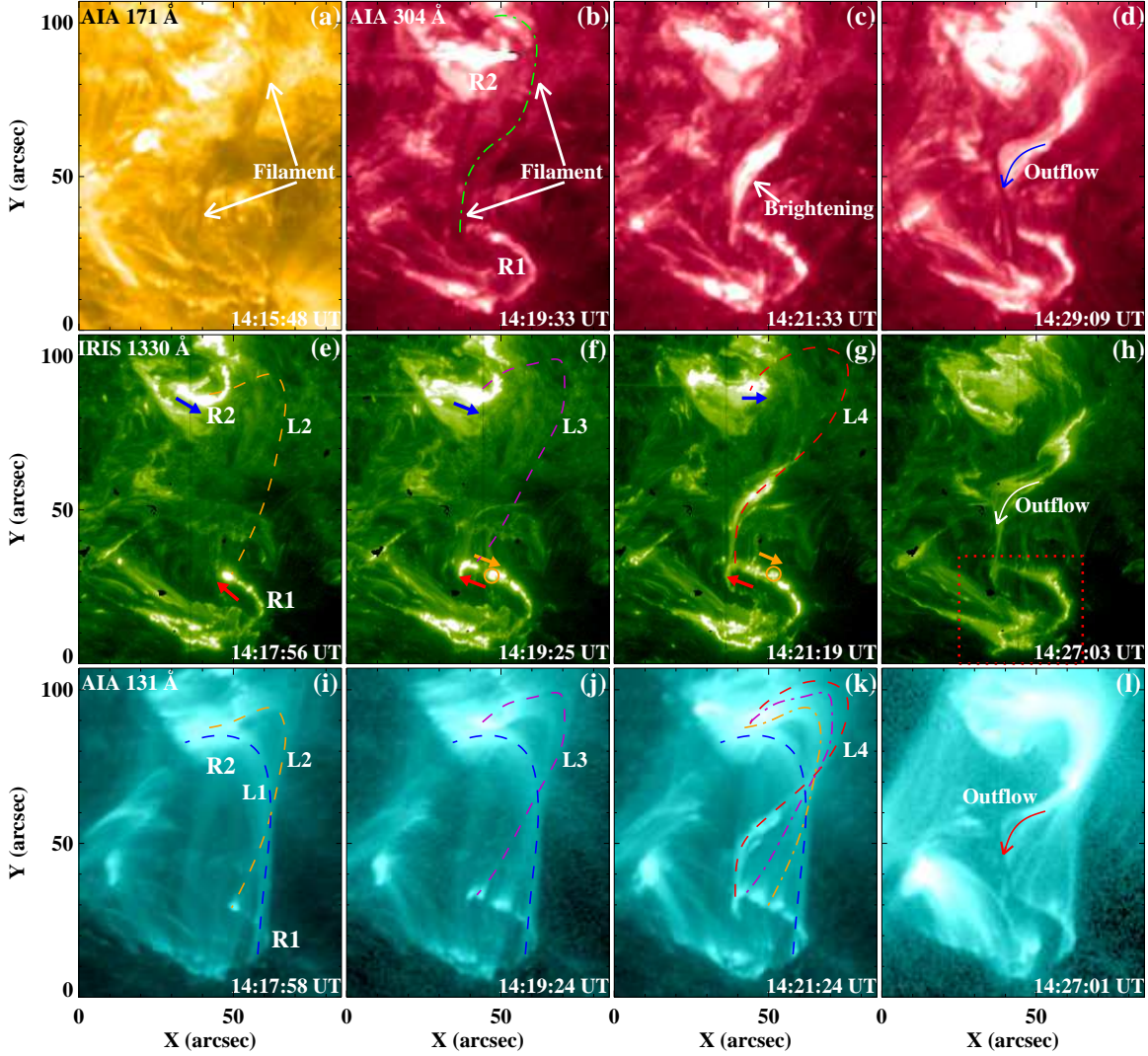


Fig. 2.— Multi-wavelength (E)UV images from the *SDO*/AIA and *IRIS* showing the dynamic evolution of the flare. The AIA images are rotated by 90° counterclockwise to co-align with the *IRIS* SJIs. The green dash-dotted curve in panel (b) outlines the filament involved in the event. The red arrows in panels (e)-(g) show the slippage of ribbon R1 towards the north, and the brown circles and arrows denote one of moving substructures within ribbon R1 and its opposite slipping direction. Blue arrows in panels (e)-(g) denote the elongation direction of ribbon R2. Dashed lines in panels (i)-(k) outline the high-temperature flare loops connecting ribbons R1 and R2, and dash-dotted lines are the duplicates of the flare loops at earlier times. The duplications of loops L2-L4 are also shown in panels (e)-(g). The red rectangle in panel (h) shows the FOV of the 1330 Å images in Figure 3. The associated animation includes *IRIS* 1330 Å, AIA 304 Å, 171 Å and 131 Å images from about 14:12 UT to 15:00 UT.

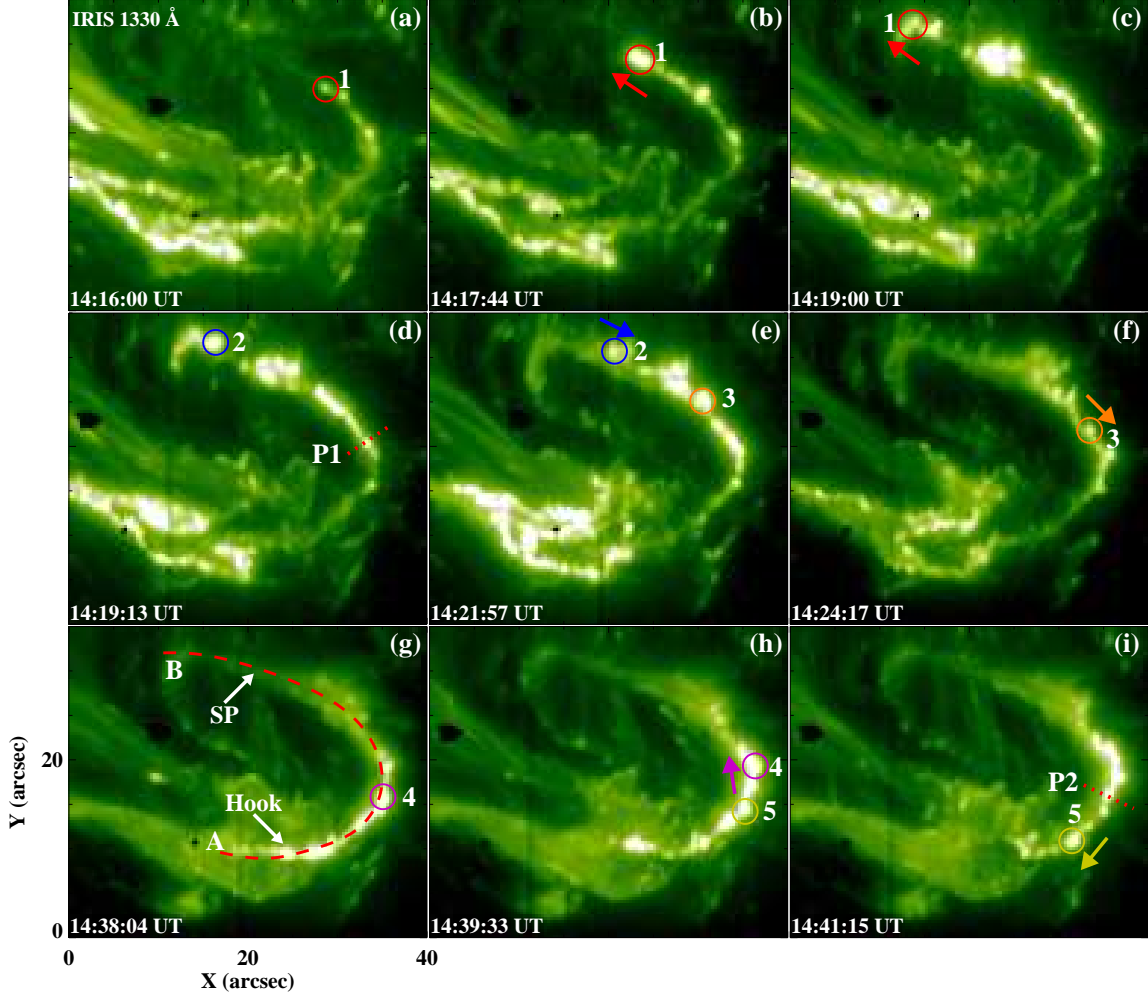


Fig. 3.— Time series of 1330 Å images showing the bi-directional slippage of the substructures within ribbon R1. The circles with different colors show five of slipping substructures (“1” – “5”), and the arrows point to the slipping directions. Dotted lines “P1” in panel (d) and “P2” in panel (i) denote the two cuts shown in Figures 4(c)-(d). Dashed curve “A-B” (panel (g)) represents the location used to obtain the stack plot shown in Figure 4(a). “A” is at the hook part of the ribbon and “B” is at the straight part (SP) near the inversion line. The associated animation includes the zoomed *IRIS* 1330 Å images, starting at 14:11:59 UT and ending at 15:04:49 UT.

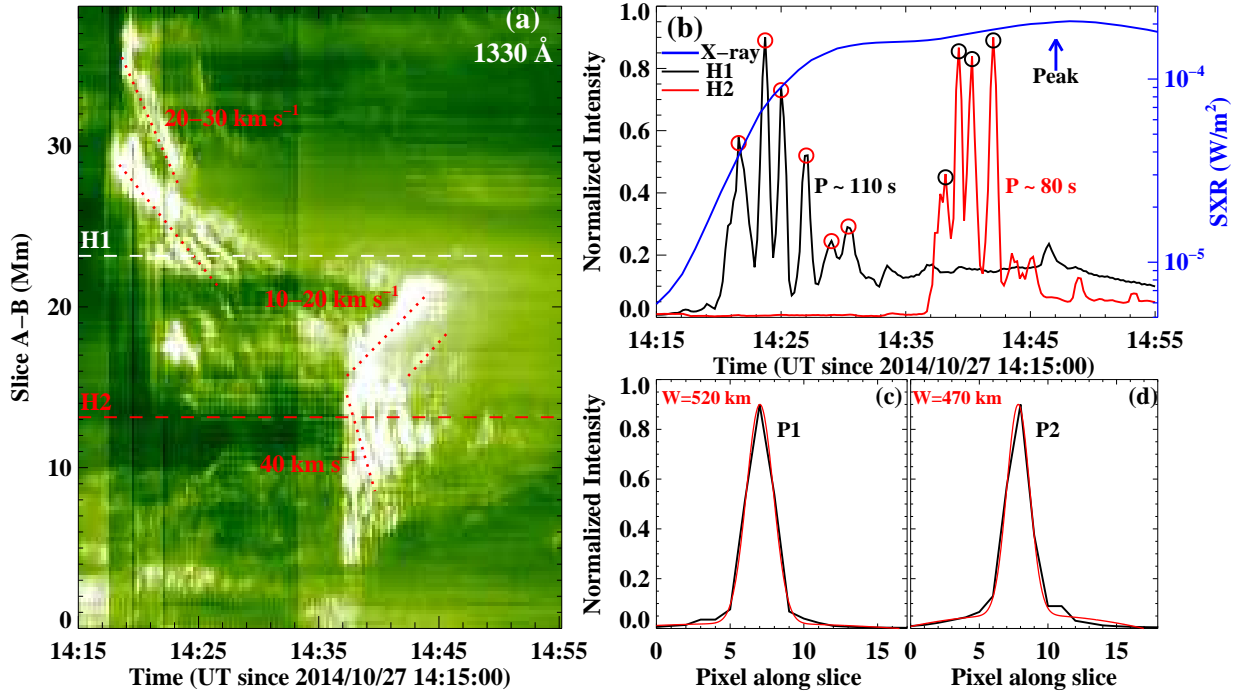


Fig. 4.— Panel (a): 1330 Å stack plot along slice “A-B” (Figure 3(g)) displaying the quasi-periodic slipping motion of ribbon substructures. Two horizontal lines “H1” and “H2” denote the locations where the horizontal slices in panel (b) are obtained. Panel (b): GOES SXR 1-8 Å flux (blue curve) of the flare and horizontal slices (black and red curves) along straight lines “H1” and “H2”. Panels (c)-(d): intensity-location profiles (black curves) and their Gaussian fitting profiles (red curves) along the two cuts “P1” and “P2” (Figures 3(d) and (i)) showing the widths (W) of the substructures.

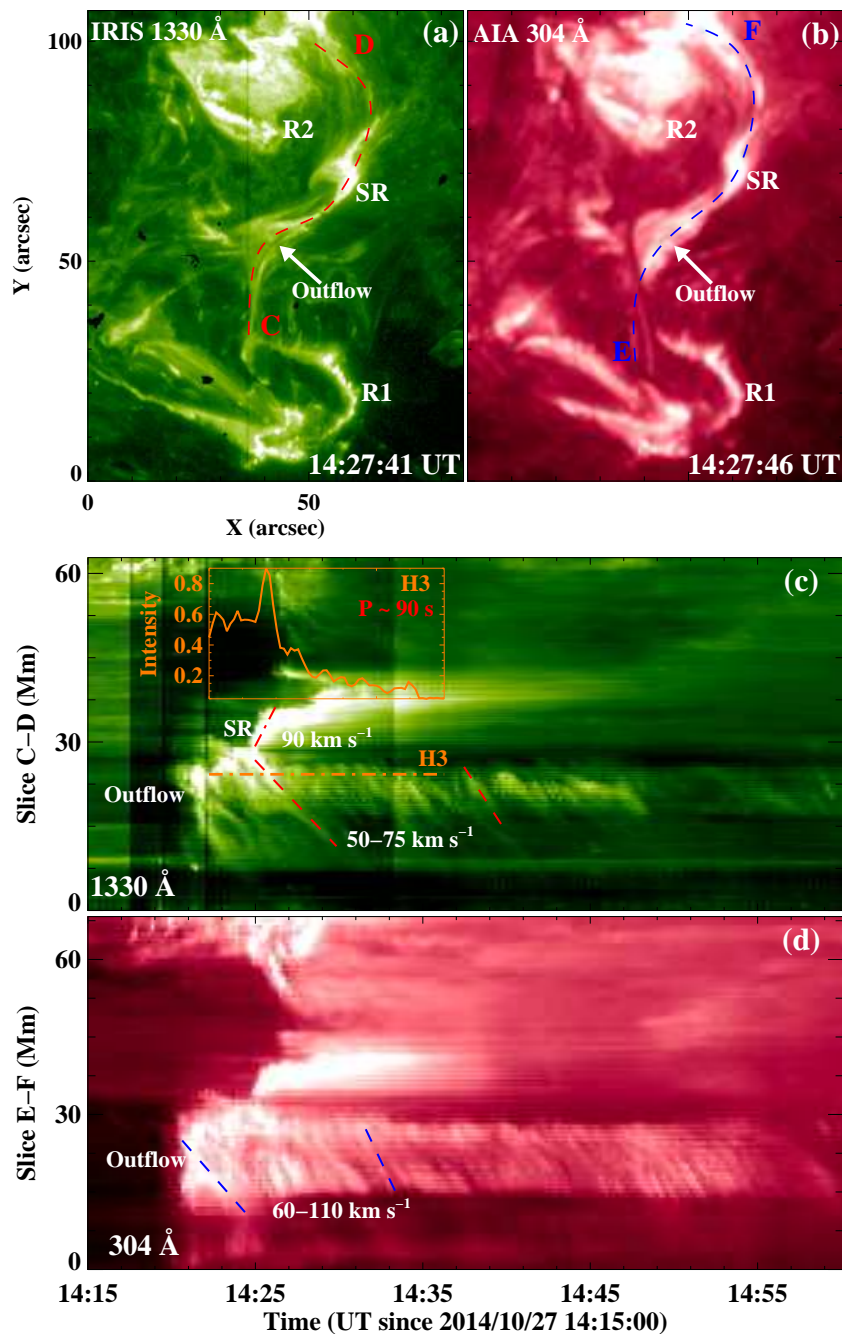


Fig. 5.— Continual reconnection-induced flows along the non-eruptive filament in 1330 and 304 Å observations. The FOV of panels (a)-(b) is the same as the images in Figure 2. The red and blue curves (“C-D” and “E-F”) in panels (a)-(b) respectively denote the locations where the two stack plots in panels (c)-(d) are obtained. SR in panels (a)-(c) represents the secondary ribbon between the two ribbons R1 and R2. The overplotted brown curve in panel (c) shows the normalized intensity along the horizontal brown dash-dotted line “H3”.

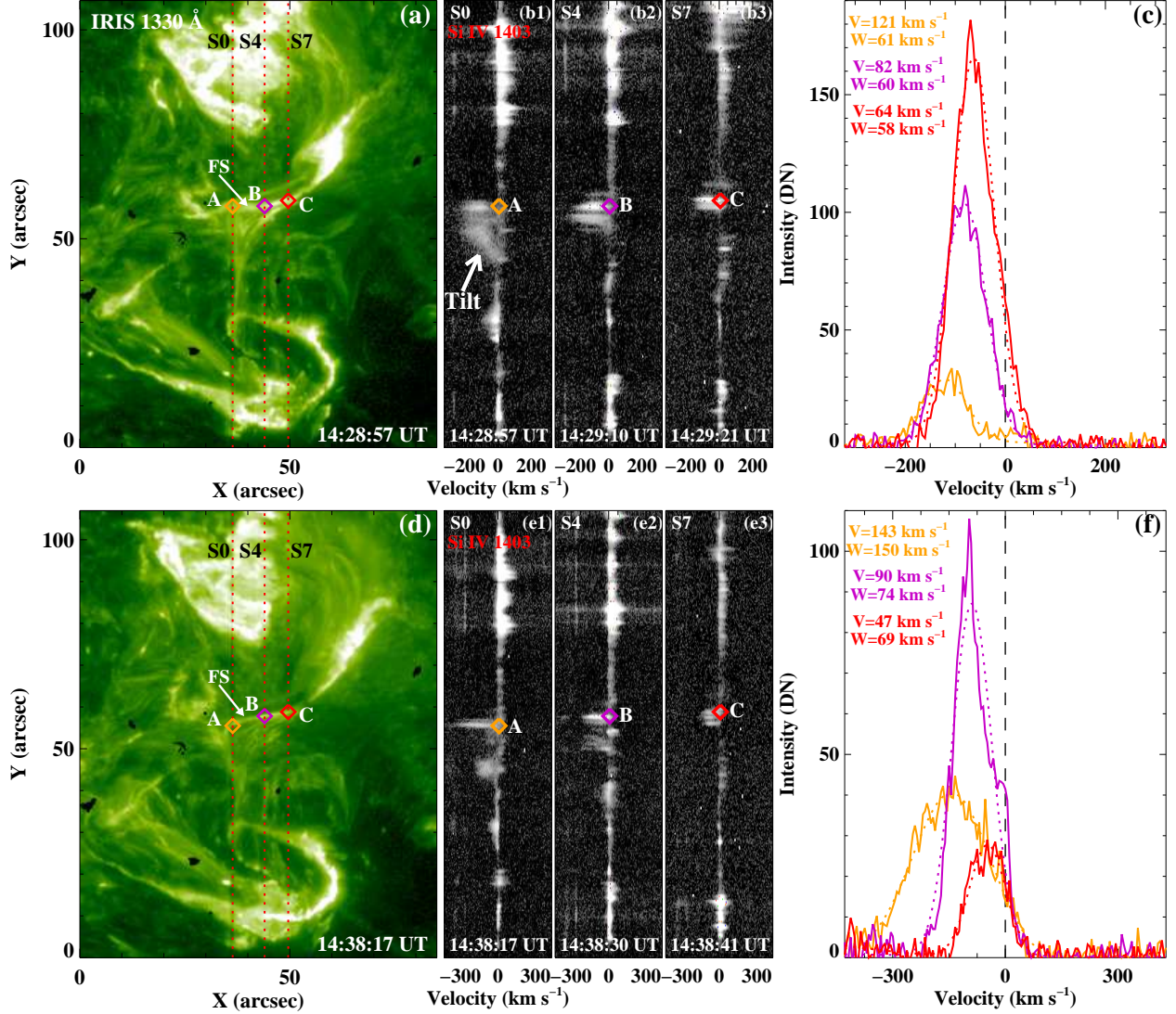


Fig. 6.— Left column: *IRIS* 1330 Å SJI images displaying the slit locations and the fine structure of the filament (FS). Their FOV is the same as Figure 2. The red dotted lines denote three slit locations S0, S4 and S7, and the diamonds (“A”, “B” and “C”) show three selected locations along the structure FS of the filament. Middle column: spectral images of the Si IV 1402.77 Å at the three slits as shown in panels (a) and (d). Right column: profiles of the Si IV line at locations “A”, “B” and “C”. The solid curves are the observed profiles and the dotted curves are single-Gaussian fitting profiles.

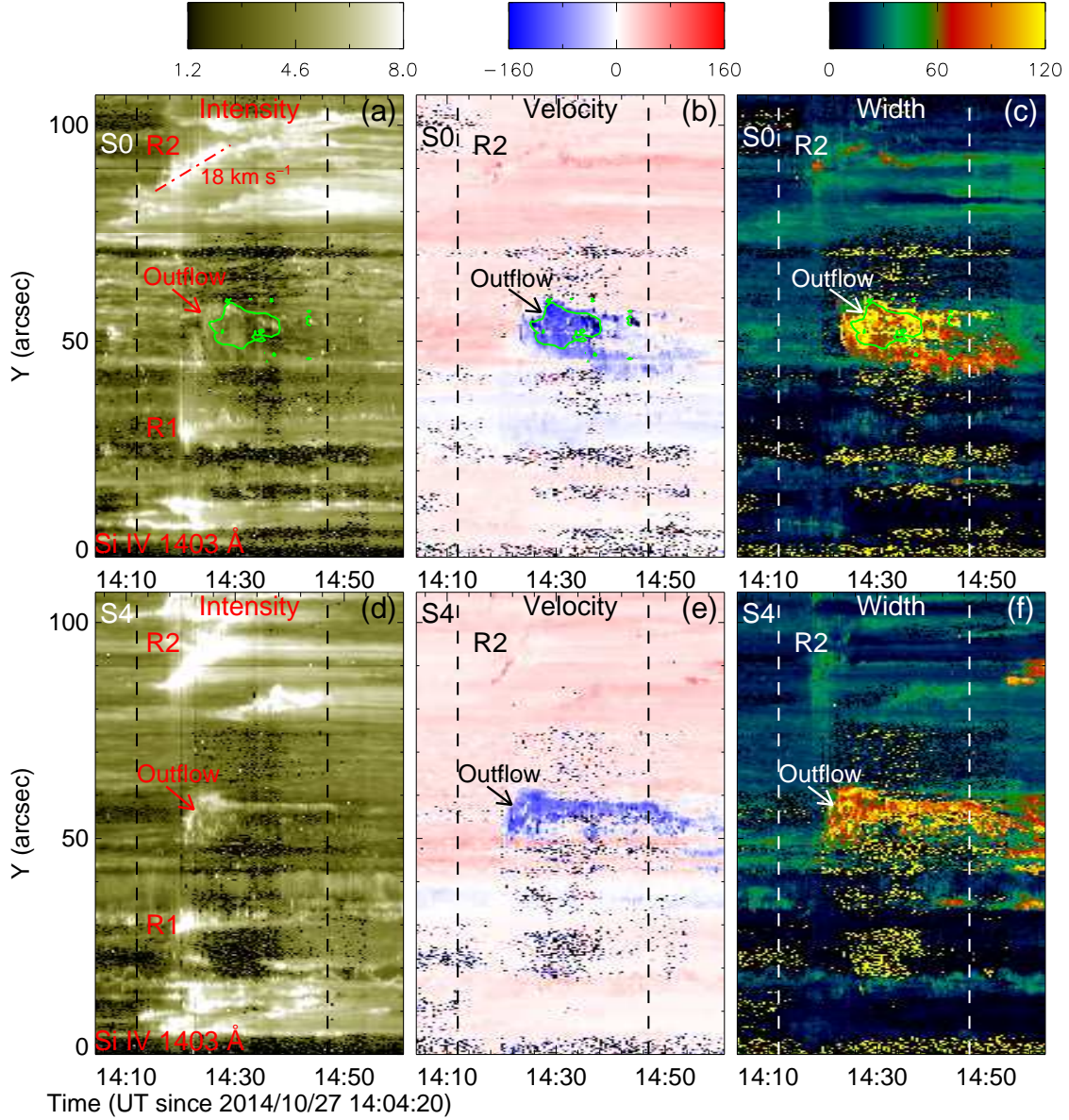


Fig. 7.— Top row: temporal evolution of peak intensity, Doppler shift and non-thermal width through fitting the Si IV profiles along S0. The spatial range is along the Y axis in Figures 6(a) and (d). The green contours are the Doppler blueshifts at the level of 80 km s^{-1} . Two dashed lines respectively denote the flare start (14:12 UT) and peak time (14:47 UT). Bottom row: the same as the top row but for S4.